Tunable electron-phonon coupling superconductivity in platinum diselenide

Cai Cheng,[1,2] Jia-Tao Sun,[1,*] Min Liu,[2] Xiang-Rong Chen,[2,†] and Sheng Meng[1,‡]

[1]*Institute of Physics, Chinese Academy of Sciences, Beijing 100190, China*
[2]*Institute of Atomic and Molecular Physics, College of Physical Science and Technology, Sichuan University, Chengdu 610064, China*

The superconducting property of platinum diselenide ($PtSe_2$), being a type-II Dirac semimetal, doped with electron and hole carriers has been investigated by first-principles calculations. It is found that the superconducting transition temperature T_c of pristine $PtSe_2$ is very low ($\leqslant 0.002$ K), making it infeasible as a practical superconductor. The electron doping is an effective way to increases the T_c of $PtSe_2$ to 2.15 K at $0.5e^-$ per unit cell. We further find that the mechanism of superconducting transition is the acoustic branch vibration mode softening rather than the Fermi surface nesting. Our results provide an important clue to increase superconducting temperature in the heavy transition-metal dichalcogenides and shed light on searching for new superconducting topological semimetals.

I. INTRODUCTION

Layered transition-metal dichalcogenides (TMX$_2$, M $=$ metal, X $=$ S,Se,Te) have attracted intensive attention, thanks to the fact that they serve as playgrounds for diverse fundamental phenomena including charge-density wave [1], superconductivity [2], and for potential applications such as field-effect transistors [3], phototransistors [4], and valleytronics [5–8]. The molybdenum and tungsten disulfides are among the most-studied dichalcogenide materials, which exhibit moderate band gap in the visible and near-infrared region [9,10], a reasonable carrier mobility of $200\,cm^2\,V^{-1}\,s^{-1}$ with very good on-off current ratio [11], and excellent electrostatic integrity [12,13]. Currently the family of TMX$_2$ materials extends beyond these earlier found molybdenum or tungsten dichalcogenides. Platinum diselenide ($PtSe_2$) has emerged as an important compound of great interest in this class. Although bulk 1T-$PtSe_2$ crystal is a type-II Dirac semimetal [14,15], its monolayer (ML) is a semiconductor with an indirect band gap of 1.2 eV obtained by density-functional theory calculations based on local-density approximation [16]. When the layer thickness of $PtSe_2$ is further increased, the $PtSe_2$ thin films show a distinct layer-dependent semiconductor-to-semimetal evolution, making it suitable for constructing a versatile air-stable 2D field-effect transistor [17]. The strong band-gap dependence in van der Waals stacking $PtSe_2$ thin film originates from the coupling of the out-of-plane front orbitals of the top valence band and bottom conduction band [18]. Moreover, the hidden helical spin texture with spin-layer locking in ML $PtSe_2$ has been recently revealed [19]. Such spin physics inducing a local Rashba effect possesses a great potential for building electric-field-tunable spintronic devices.

Experimentally, ML $PtSe_2$ has been grown by direct selenization of Pt(111) substrate at low temperatures [16], which is easy to fabricate thin films of sizes up to millimeter scale. $PtSe_2$ can also be grown by chemical vapor deposition [20] and thermally assisted conversion [21]. Recently, the high-quality atomically thin $PtSe_2$ films have been grown by molecular-beam epitaxy (MBE) [22], which provides new opportunities for investigating the physical properties and potential applications of $PtSe_2$ for room-temperature electronic devices with high electron mobility [23,24]. Manchanda *et al.* [25] predicted that hydrogenation transforms the semiconducting Pt dichalcogenides monolayers into ferromagnetic metals whose magnetic moment mainly originates from Pt $5d$ electrons. Monolayer $PtSe_2$ is also useful for gas sensing [26] due to the high adsorption energies for gaseous molecules (NO_2, NO, NH_3, H_2O, CO_2, and CO molecules, etc.) on the surface. Recently, numerous works have been carried out to investigate the novel physical properties of $PtSe_2$ and related materials [27–32]. The isostructural $PdTe_2$ is also shown to be a type-II Dirac semimetal with a superconducting transition temperature $T_c = 1.7$ K [33,34]. However, the mechanism of superconducting transitions in these exotic type-II Dirac semimetal materials is unclear. It is thus worthy to explore the superconducting property for the type-II Dirac semimetal $PtSe_2$ thanks to the fact that high-quality samples have been grown by MBE [16,22].

In this work, we present a detailed study on the carrier-concentration-dependent superconducting properties in bulk $PtSe_2$ by accurate first-principles calculations. Our results show that the undoped $PtSe_2$ has an extremely low superconducting transition temperature T_c of 0.002 K. The electron doping can effectively achieve the Bardeen, Cooper, and Schrieffer (BCS)-type superconductor mediated by effective electron-phonon coupling with a higher $T_c = 2.15$ K by doping $0.5e^-$ per formula unit cell. Furthermore, we find that the mechanism of increasing superconducting transition temperature is related to the softening of acoustic vibrational modes rather than the Fermi surface nesting. Our results provide an important clue to explore novel superconductivity in the $PtSe_2$ class of type-II Dirac semimetals.

II. METHODS

We have performed density-functional theory calculations based on the plane-wave code QUANTUM ESPRESSO [35] adopting the local-density approximation (LDA) [36,37]. The plane-wave pseudopotentials were used to treat the

---

*Corresponding author: jtsun@iphy.ac.cn
†Corresponding author: xrchen@scu.edu.cn
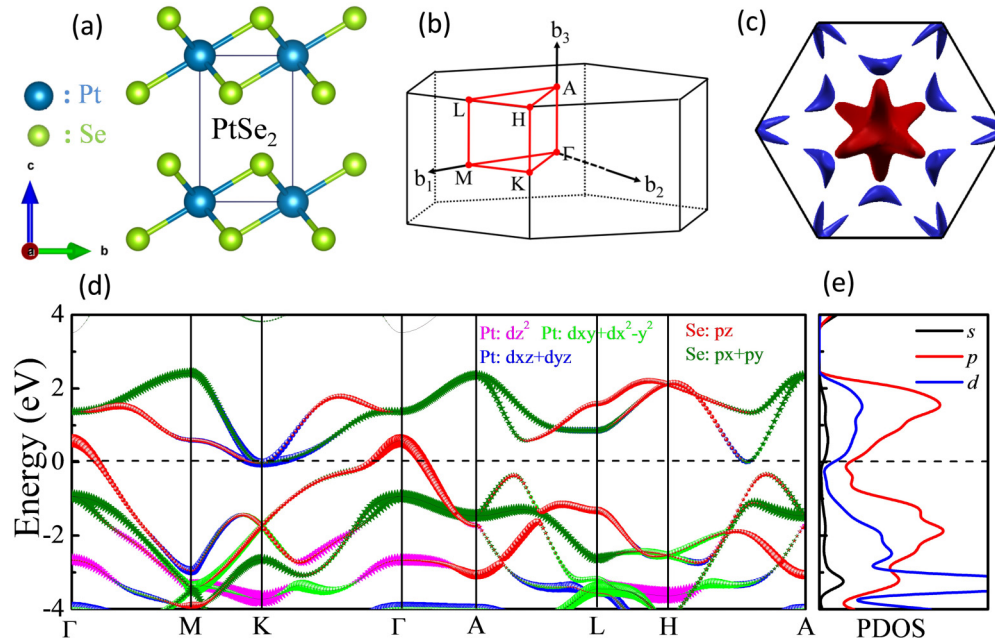‡Corresponding author: smeng@iphy.ac.cn

FIG. 1. Atomic structure and electronic structure of PtSe$_2$. (a) Atom structure of bulk PtSe$_2$ with $P\bar{3}m1$ symmetry. (b) Brillouin zone of bulk PtSe$_2$. (c) Fermi surface of bulk PtSe$_2$ without SOC. (d) Band structure of bulk PtSe$_2$ without SOC. The fatted bands with spectral weight of Pt d_{z^2}, $d_{xy} + d_{x^2+y^2}$, and $d_{xz} + d_{yz}$ orbitals and Se $p_x + p_y$ and p_z orbitals. (e) Partial density of states.

electron-ion interactions. After the full convergence test, the plane-wave cutoff and the charge-density cutoff of the plane-wave basis were chosen to be 60 and 240 Ry, respectively. The Gauss smearing width of 0.005 Ry was used. The self-consistent electron density in bulk PtSe$_2$ was evaluated on a $16 \times 16 \times 16$ k-point grid. The dynamic matrix and electron-phonon coupling (EPC) matrix elements were calculated on a $4 \times 4 \times 4$ grid. Eventually, finer grids of $32 \times 32 \times 32$ were used to accurately determine the electron-phonon coupling strength in bulk PtSe$_2$. The lattice constants after full atomic relaxation were adopted. The phonon properties and electron-phonon coupling were calculated based on density-functional perturbation theory [38] and the Eliashberg equation [39,40] in the Supplemental Material [41].

III. RESULTS AND DISCUSSION

A. Atomic structure and electronic properties of bulk PtSe$_2$

Bulk PtSe$_2$ has a stable $1T$ phase corresponding to the CdI$_2$-type trigonal structure with $P\bar{3}m1$ space group (no. 164, D_{3d}). PtSe$_2$ has a layered structure with weak interlayer interactions. In each layer, Pt atoms are sandwiched by top and bottom Se layers with inversion symmetry, where the Pt atoms are octahedrally coordinated by the Se atoms. We fixed $c/a = 1.361$ to the experimental value and relaxed the lattice constant a, then obtained the minimum energy E_0 together with the lattice parameter $a = 3.71$ Å and $c = 5.05$ Å, which are very close to the experimental values ($a = 3.73$ Å, $c = 5.08$ Å) [42–44] and calculations ($a = 3.73$ Å, $c = 5.08$ Å) [45]. All the results below are based on the optimized lattice constant. The atomic structure of bulk PtSe$_2$ is shown in Fig. 1(a). The bulk hexagonal Brillouin zone is shown in Fig. 1(b), where the high-symmetry points and lines are indicated by red color. Figure 1(c) shows the Fermi surface of the bulk

PtSe$_2$ without spin-orbit coupling (SOC), where there are six pairs of electron and hole pockets. Figure 1(d) shows the band structure, which presents the projected bands with spectral weight of Pt d_{z^2}, $d_{xy} + d_{x^2+y^2}$, and $d_{xz} + d_{yz}$ orbitals (colored by magenta, green, and blue, respectively) and Se $p_x + p_y$ and p_z orbitals (colored by olive and red, respectively). It explicitly exhibits the semimetallic characteristics, where both electron and hole pockets coexist at the Fermi surface. It is also obvious that the reported type-II Dirac fermions [14] along the ΓA direction are mainly composed of the hybrid $p_x + p_y$ and p_z orbitals of Se atoms. Figure 1(e) shows the corresponding partial density of state (PDOS), which exhibits that the Fermi surface is mainly composed of Se p orbital partially hybridized with Pt d ($d_{xz} + d_{yz}$) orbitals. More details about PDOS are shown in Fig. S1 (Supplemental Material [41]). Figure S1 exhibits the three-pair degenerate orbitals of p_x and p_y, d_{xz} and d_{yz}, d_{xy} and $d_{x^2+y^2}$, which is the base of the fatted band structure in Fig. 1(d).

B. Phonon-mediated superconductivity in PtSe$_2$

To explore the possible superconductivity induced by electron-phonon coupling in pristine bulk PtSe$_2$, we calculate phonon dispersion including the EPC, Eliashberg spectral functions, and phonon density of states for PtSe$_2$ as shown in Fig. 2. The size of the red dots is proportional to the EPC constants (λ_{qv}) for a specific phonon mode qv. There is no imaginary phonon mode in the phonon dispersion [Fig. 2(a)], indicating that pristine bulk PtSe$_2$ is dynamically stable. Particularly, there is a dip in the lower acoustic phonon branches in the middle region along the Γ-K path, where the electron-phonon coupling is ten times larger than those in other frequency regions. Furthermore, we have observed a visible gap of $11 \, \text{cm}^{-1}$ in optical phonon branch frequency
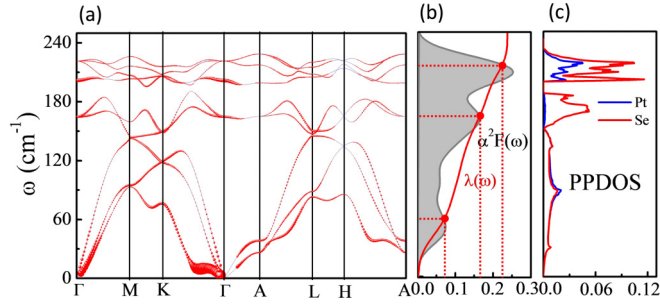
FIG. 2. Phonon dispersion, Eliashberg spectral function and the frequency-dependent electron-phonon coupling parameter. (a) Phonon dispersion and electron-phonon coupling of bulk $PtSe_2$. The size of the circles is proportional to the magnitude of electron-phonon coupling λ_{qv}. (b) Calculated Eliashberg spectral function $\alpha^2 F(\omega)$ and $\lambda(\omega)$ (c) PPDOS contributed by Pt and Se atoms separately.

between 187 and 198 cm^{-1} and a zero-contact point between acoustic and optical phonon branch in the high symmetry points of M and L. Figure 2(c) shows three regions of the partial atomic phonon density of states (PPDOS): (I) $0 \sim 146$ cm^{-1}, (II) $146 \sim 187$ cm^{-1}, and (III) $198 \sim 232$ cm^{-1}. Region I shows strong mixing of Pt atoms and Se atoms with almost equal contributions, since the acoustic phonon branches comprise collective lattice motion of all atoms. However, region II is completely dominated by vibrations of the Se atoms, which is essential due to the smaller mass of atom Se. Moreover, the partial atomic phonon density of states in region III is mostly dominated by the variations of Se atoms and the partial hybridization contributions of Pt atoms. The Raman peaks have been measured in the experiments [15,22], where the E_g mode (about 180 cm^{-1}) involves the in-plane vibration with the upper and bottom Se atoms moving in opposite directions, and the A_{1g} mode (205 cm^{-1}) corresponds to the out-of-plane vibration of Se atoms. The experimental Raman peak positions are consistent well with our results. For details of vibrational patterns for each mode, refer to Refs. [15,22].

The calculated Eliashberg spectral function $\alpha^2 F(\omega)$ and the integrated λ_{qv} are shown in Fig. 2(b). As we can see, the Eliashberg spectral function has three major peaks in the whole frequency region, which can be approximately divided into three parts. From Fig. 2(b), we find that the low-energy phonon region ($0 \sim 58$ cm^{-1}) contributes partially to electron-phonon coupling in bulk $PtSe_2$, as they account for 29.3% of the total EPC constant. The middle-energy region ($58 \sim 165$ cm^{-1}) has the largest contribution (43.1%) to the electron-phonon coupling. The high-energy phonon modes ($165 \sim 232$ cm^{-1}) contribute to the remaining weight (27.6%) of the EPC. By employing the quasi-harmonic approximation (QHA) [46] implemented in the QUANTUM ESPRESSO package, the Debye temperature (Θ) of $PtSe_2$ is obtained as 305 K, which is larger than the value of 229 K directly evaluated by elastic constant Debye temperature. These results can be further validated in future experiments.

In addition, we also show the effect of SOC on the band structure, phonon dispersion, and superconductivity-related physical quantities in Fig. S2 (Supplemental Material [41]) and Table S1 (Supplemental Material [41]). We find that the SOC

effect is negligible on the phonon dispersion of the pristine bulk $PtSe_2$. Besides, the energy-band splitting of 0.18 eV is induced by the SOC effect on the band structure. The Fermi surface does not change significantly with the inclusion of SOC. In addition, the calculated T_c with electron doping is slightly affected by SOC.

C. Electronic structure and phonon dispersion under carrier doping

Charge-carrier doping can be generally applied to control the electronic properties for exploring the superconductivity of bulk materials, which has been successfully realized in a variety of systems such as $Cu_x Bi_2 Se_3$, $Cu_x TiSe_2$, etc. [1,47,48] The carrier doping is simulated by directly adding electrons into or removing electrons from the system, together with a compensating uniform charge background of opposite sign to maintain charge neutrality [49,50]. We studied the effects of carrier doping on the superconducting properties in bulk $PtSe_2$. For each doping concentration, we relaxed the atomic degree of freedom (DOF) of bulk $PtSe_2$ except the lattice DOF.

Figure 3(a) shows the electronic properties of bulk $PtSe_2$ under carrier doping in the concentration of $0.3e^-$/cell (red), $0.5e^-$/cell (blue), and $0.3h^+$/cell (cyan). Data for pristine undoped bulk $PtSe_2$ (black line) are also presented for comparison. The black dashed line is the Fermi level and the Fermi level of each case has been set to 0. The general dispersion of band structures remains almost unchanged, while the whole profile moves downward with the increasing electron doping concentration, leading to smaller hole pockets and larger electron pockets. In the meantime, the energy E_D of type-II Dirac point along the ΓA direction decreases with the increasing doping level.

The calculated phonon-dispersion spectra of bulk $PtSe_2$ under carrier doping are shown in Fig. 3(b); the details of the weight including electron-phonon coupling under carrier doping also shown in Fig. S3 (Supplemental Material [41]), where the color symbols are same as those in Fig. 3(a). It is clear that the phonon dispersion under carrier doping has no imaginary phonon modes, indicating that carrier-doping bulk $PtSe_2$ are dynamically stable. We also note that the electron doping strongly alters the vibrational properties of the doped system as indicated by the softened frequency mode along the MK and AH direction (dotted green rectangle) with the increasing doping level. However, the phonon mode around the Γ point becomes stiff with the increasing doping level, which may be due to the acoustic sum rule with the different convergence at the Γ point. Moreover, in the highest-frequency region (dotted green rectangle) at the A point, vibration becomes hardened with the increasing doping level.

The dependence of the Eliashberg phonon spectral function $\alpha^2 F(\omega)$ on carrier doping is shown in Fig. 3(c). As we can see, the whole profile of the Eliashberg spectral function $\alpha^2 F(\omega)$ moves to a lower-frequency region with the increasing electron doping level. The intensity of the Eliashberg spectral function is largely increased because of the increasing electron doping level. Moreover, we find that the acoustic mode (below 159 cm^{-1}) contributes to the main EPC λ under the high doping concentration (see Fig. S4 in Supplemental Material [41]).

Figure 3(d) shows the EPC λ and DOS as a function of carrier-doping concentration. When $0.3h^+$/cell (corresponding
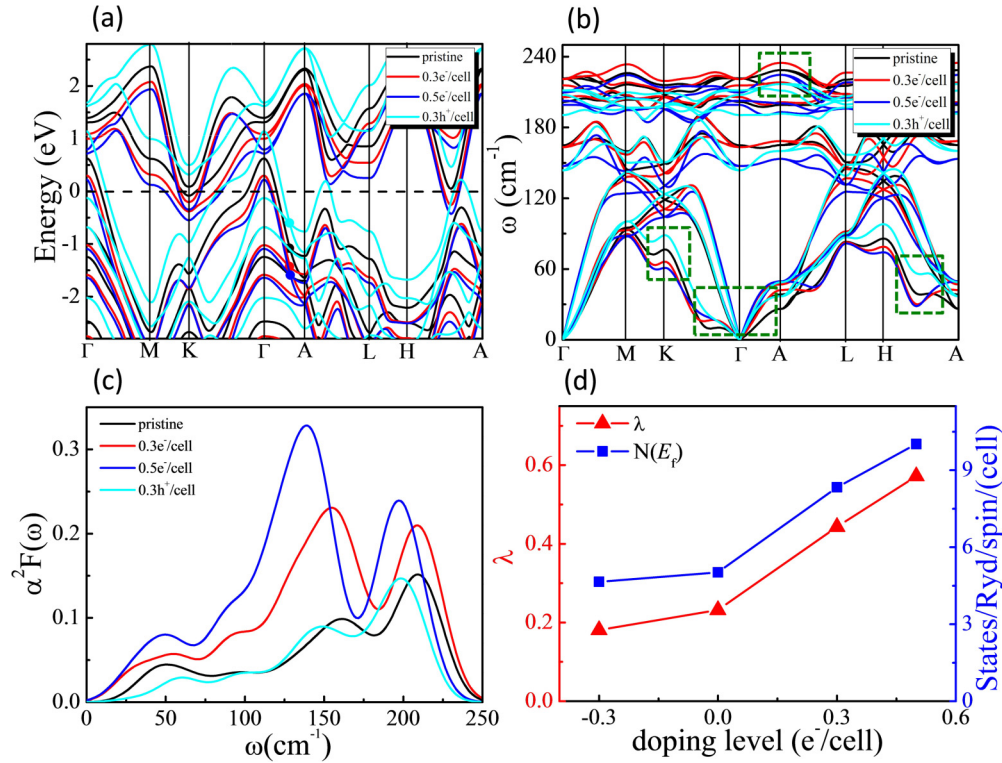
FIG. 3. Electronic band structure, phonon dispersion, Eliashberg spectral function, and the electron-phonon coupling parameter of bulk PtSe$_2$ as a function of carrier doping. (a) Band structures for bulk PtSe$_2$ doped by $0.3e^-$/cell (red), $0.5e^-$/cell (blue), and $0.3h^+$/cell (cyan). (The black dashed line is the Fermi level, which has been set to zero for each doping case.) (b) Phonon dispersion relation for bulk PtSe$_2$ doped by $0.3e^-$/cell (red), $0.5e^-$/cell (blue), and $0.3h^+$/cell (cyan). (c) Eliashberg spectral function $\alpha^2 F(\omega)$ doped by $0.3e^-$ (red), $0.5e^-$ (blue), and $0.3h^+$ (cyan) per unit cell, respectively. (d) Doping dependence of electron-phonon coupling constant λ (red) and electronic density of states at Fermi level N(E_f) (blue). In (a)–(c), pristine bulk PtSe$_2$ (black line) is presented for comparison.

to a hole density of 4.98×10^{21} cm^{-3}) is doped, the calculated N(E_f) and λ is about 4.41 states/Ryd/spin/(unit cell) and 0.181, respectively. When increasing electron doping to $0.3e^-$/cell doping, the N(E_f) increase to 8.15 states/Ryd/spin/(unit cell), and the λ becomes 0.418. Further increasing doping will generally increase the N(E_f) and λ. It seems that the electronic density of states and λ have a strong dependence on the carrier concentration. Even higher doping can lead to structural instability, which may be due to the lattice expansion under higher doping concentration. Moreover, we also show the SOC effect on the superconductivity-related physical quantities in Table S1 (Supplemental Material [41]). From Table S1, we can see that physical quantities related to superconductivity are slightly affected by spin-orbit coupling. For the strongest affected case doped with 0.5 electrons per unit cell, the calculated T_c with spin-orbit coupling included only changes from 1.81 to 2.15 K. In addition, we also studied the effect of the van der Waals forces on the physical properties by changing the value of lattice constant c. Band structure, phonon dispersion, and superconductivity-related physical quantities are shown in Fig. S5 (Supplemental Material [41]) and Table S2 (Supplemental Material [41]). We conclude that the logarithmically averaged frequency $\omega_{\log}$ and N(E_f) are slightly increased with suitable compressive strain, but the superconducting transition temperature T_c is almost unchanged.

D. Fermi surface nesting under doping

In order to tell the mechanism of superconducting transition is vibration model softening under doping or Fermi surface nesting, we also calculate the Fermi surface nesting factor (imaginary part of susceptibility) $\chi(\boldsymbol{q})$ in the static limit,

$$\chi(\boldsymbol{q}) = \sum_{\boldsymbol{k},n,m} \delta(\varepsilon_{\boldsymbol{k},n} - E_f)\delta(\varepsilon_{\boldsymbol{k+q},m} - E_f), \quad (1)$$

where $\varepsilon_{\boldsymbol{k}}$ and $\varepsilon_{\boldsymbol{k+q}}$ are the band energies and E_f is the Fermi energy. The $\chi(\boldsymbol{q})$ indicates the amounts of electronic states at the Fermi surface connected by a fixed wave vector $\boldsymbol{q}$ and reflects the Fermi surface topology. The Fermi surfaces shown in Fig. 1(c) are plotted by interpolating a 14-orbital tight-binding Hamiltonian to reproduce LDA band structure using the maximally localized Wannier function (MLWF) [51,52]. The band structure fitted by MLWFs are shown in Fig. S6 (Supplemental Material [41]). More details about Wannier orbital information are shown in Fig. S7 (Supplemental Material [41]). The obtained Hamiltonian in the Wannier basis is employed to calculate the Fermi surface nesting factor $\chi(\boldsymbol{q})$ [53]. The k mesh and the q mesh are $600 \times 600 \times 1$ and $150 \times 150 \times 1$, respectively.

Figure 4 shows the Fermi surface nesting $\chi(\boldsymbol{q})$ in the Brillouin zone under carrier-doping level with $0.3h^+$/cell, pristine, $0.3e^-$/cell, $0.5e^-$/cell, respectively. It is obvious that
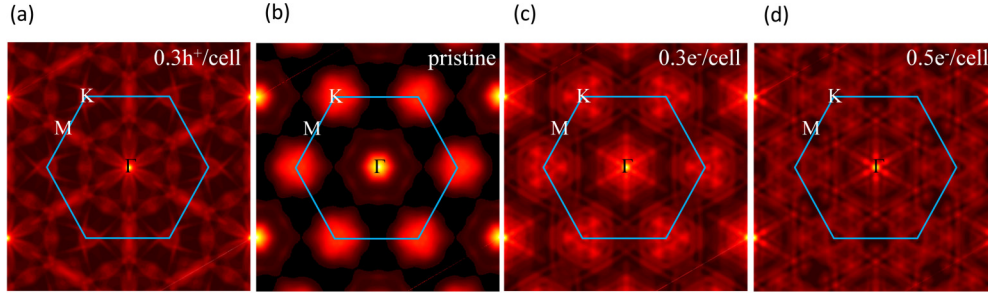
FIG. 4. Fermi surface nesting evolution as a function of carrier concentration. (a)–(d) Fermi surface nesting under carrier-doping level of $0.3h^+$, pristine, $0.3e^-$, and $0.5e^-$ per unit cell, respectively.

the contribution of Fermi surface nesting is small except for the Γ point and the K point, which exhibit the hole pocket and electron pocket of the Fermi surface, respectively. The weakening of $\chi(\boldsymbol{q})$ near the Γ center with the increasing doping level comes from the fact that when the hole pocket becomes smaller, the amounts of electronic states at the Fermi surface decrease. This evidences the mechanism of Kohn anomaly, rather than Fermi surface nesting, for the occurrence of the superconductivity.

E. Tuning superconducting transition temperature

The evaluation of the critical superconducting transition temperatures T_c is based on the microscopic theory of BCS [54,55], with the rigorous treatment of electron-phonon interactions introduced by Migdal [56] and Eliashberg [39]. Phonon frequencies and electron-phonon coupling coefficients are calculated using density-functional perturbation theory. The actual T_c values reported here are obtained from the analytical approximation given by the McMillan equation [57], further modified by Allen and Dynes [58,59]:

$$T_c = \frac{\omega_{\log}}{1.2} \exp\left[\frac{-1.04(1+\lambda)}{\lambda(1-0.62\mu^*) - \mu^*} \right], \qquad (2)$$

where the $\omega_{\log}$ is the logarithmically averaged frequency given by

$$\omega_{\log} = \exp\left[\frac{2}{\lambda} \int \frac{d\omega}{\omega} \alpha^2 F(\omega) \log\omega \right]. \qquad (3)$$
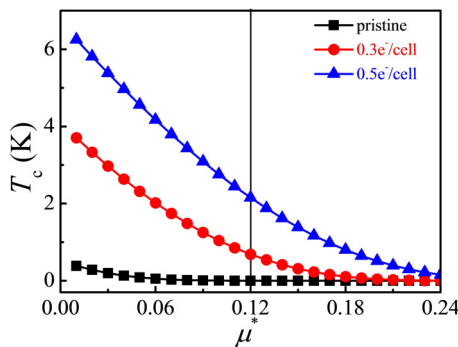

FIG. 5. Evaluated superconducting transition temperature T_c of bulk $PtSe_2$ as a function of Coulomb pseudopotential μ^*. Vertical line marks the value $\mu^* = 0.12$ used in this work.

Here, μ^* is an effective screened Coulomb potential which cannot be determined by the first-principles calculation and usually is assumed to take a value between 0.1 and 0.15 [60,61] ($\mu^* = 0.12$ in this work).

The superconducting transition temperature T_c is estimated to be of an extremely low temperature of 0.002 K for pristine $PtSe_2$. Our calculations show, however, that λ and T_c increase significantly when doping bulk $PtSe_2$ with electrons (or, equivalently, raising the Fermi level). We calculated λ and T_c at several doping levels as shown in Figs. 3(d) and 5, respectively. The results in Fig. 5 suggest a monotonic increase of the superconducting critical temperature on raising the Fermi level. For example, when adding 0.5 electrons to the unit cell, the calculated T_c with spin-orbit coupling is to become approximately 2.15 K. This effect becomes more prominent when the Fermi level shift is larger than 0.4 eV. Moreover, the calculated T_c with electron doping is slightly affected by spin-orbit coupling (see Table S2, Supplemental Material [41]). However, hole doping would decrease the superconducting transition temperature. This trend is distinct from that of the borophene in our previous work [50].

IV. CONCLUSION

In summary, we have investigated the carrier-doping effects on the electronic structure and phonon-mediated electron-phonon coupling in $PtSe_2$ by first-principles calculations. Superconducting transition temperature T_c is significantly enhanced by electron doping, which can increase to 2.15 K at the $0.5e^-$/cell-doping level. Enhancement of T_c can be achieved by softening the low-energy acoustic phonon modes and Kohn anomaly as demonstrated in the phonon dispersion spectrum. Our results provide some clues for potentially obtaining topological superconducting state in a nontrivial Dirac semimetal $PtSe_2$ by charge doping.

Supplemental Material [41] is available from the Online Library or from the author.

[1] E. Morosan, H. W. Zandbergen, B. S. Dennis, J. W. G. Bos, Y. Onose, T. Klimczuk, A. P. Ramirez, N. P. Ong, and R. J. Cava, Nat. Phys. **2**, 544 (2006).

[2] J. T. Ye, Y. J. Zhang, R. Akashi, M. S. Bahramy, R. Arita, and Y. Iwasa, Science **338**, 1193 (2012).

[3] B. Radisavljevic, A. Radenovic, J. Brivio, V. Giacometti, and A. Kis, Nat. Nanotechnol. **6**, 147 (2011).

[4] Z. Yin, H. Li, H. Li, L. Jiang, Y. Shi, Y. Sun, G. Lu, Q. Zhang, X. Chen, and H. Zhang, ACS Nano **6**, 74 (2012).

[5] D. Xiao, G.-B. Liu, W. Feng, X. Xu, and W. Yao, Phys. Rev. Lett. **108**, 196802 (2012).

[6] H. Zeng, J. Dai, W. Yao, D. Xiao, and X. Cui, Nat. Nanotechnol. **7**, 490 (2012).

[7] K. F. Mak, K. He, J. Shan, and T. F. Heinz, Nat. Nanotechnol. **7**, 494 (2012).

[8] J. Liu, W. J. Hou, C. Cheng, H. X. Fu, J. T. Sun, and S. Meng, J. Phys.: Condens. Matter **29**, 255501 (2017).

[9] R. F. Service, Science **348**, 490 (2015).

[10] H. Wang, H. Yuan, S. S. Hong, Y. Li, and Y. Cui, Chem. Soc. Rev. **44**, 2664 (2015).

[11] B. Radisavljevic and A. Kis, Nat. Mater. **12**, 815 (2013).

[12] Y. Yoon, K. Ganapathi, and S. Salahuddin, Nano Lett. **11**, 3768 (2011).

[13] K. Alam and R. K. Lake, IEEE Trans. Electron Devices **59**, 3250 (2012).

[14] H. Huang, S. Zhou, and W. Duan, Phys. Rev. B **94**, 121117(R) (2016).

[15] K. Zhang, M. Yan, H. Zhang, H. Huang, M. Arita, Z. Sun, W. Duan, Y. Wu, and S. Zhou, Phys. Rev. B **96**, 125102 (2017).

[16] Y. Wang, L. Li, W. Yao, S. Song, J. T. Sun, J. Pan, X. Ren, C. Li, E. Okunishi, Y.-Q. Wang, E. Wang, Y. Shao, Y. Y. Zhang, H. Yang, E. F. Schwier, H. Iwasawa, K. Shimada, M. Taniguchi, Z. Cheng, S. Zhou, S. Du, S. J. Pennycook, S. T. Pantelides, and H.-J. Gao, Nano Lett. **15**, 4013 (2015).

[17] Y. Zhao, J. Qiao, Z. Yu, P. Yu, K. Xu, S. P. Lau, W. Zhou, Z. Liu, X. Wang, W. Ji, and Y. Chai, Adv. Mater. **29**, 1604230 (2017).

[18] Z. Huang, W. Zhang, and W. Zhang, arXiv:1605.08536v1.

[19] W. Yao, E. Wang, H. Huang, K. Deng, M. Yan, K. Zhang, K. Miyamoto, T. Okuda, L. Li, Y. Wang, H. Gao, C. Liu, W. Duan, and S. Zhou, Nat. Commun. **8**, 14216 (2017).

[20] M. OBrien, N. McEvoy, C. Motta, J.-Y. Zheng, N. Berner, J. Kotakoski, K. Elibol, T. Pennycook, J. C Meyer, C. Yim, M. Abid, T. Hallam, J. Donegan, S. Sanvito, and G. Duesberg, 2D Mater. **3**, 021004 (2016).

[21] C. Yim, K. Lee, N. McEvoy, M. OBrien, S. Riazimehr, N. Berner, C. Cullen, J. Kotakoski, J. Meyer, M. Lemme, and G. Duesberg, ACS Nano **10**, 9550 (2016).

[22] M. Yan, E. Wang, X. Zhou, G. Zhang, H. Zhang, K. Zhang, W. Yao, S. Yang, S. Wu, T. Yoshikawa, K. Miyamoto, T. Okuda, Y. Wu, P. Yu, W. Duan, and S. Zhou, 2D Mater. **4**, 045015 (2017).

[23] W. Zhang, Z. Huang, W. Zhang, and Y. Li, Nano Res. **7**, 1731 (2014).

[24] Z. Huang, W. Zhang, and W. Zhang, Materials **9**, 716 (2016).

[25] P. Manchanda, A. Enders, D. J. Sellmyer, and R. Skomski, Phys. Rev. B **94**, 104426 (2016).

[26] M. Sajjad, E. Montes, N. Singh, and U. Schwingenschlögl, Adv. Mater. Interfaces **4**, 1600911 (2016).

[27] P. Li, L. Li, and X. C. Zeng, J. Mater. Chem. C **4**, 3106 (2016).

[28] W. Zhang, H. T. Guo, J. Jiang, Q. C. Tao, X. J. Song, H. Li, and J. Huang, J. Appl. Phys. **120**, 013904 (2016).

[29] D. Voiry, A. Goswami, R. Kappera, Cecilia de Carvalho Castro e Silva, D. Kaplan, T. Fujita, M. Chen, T. Asefa, and M. Chhowalla, Nat. Chem. **7**, 45 (2015).

[30] Y. Zhao, J. Qiao, P. Yu, Z. Hu, Z. Lin, S. P. Lau, Z. Liu, W. Ji, and Y. Chai, Adv. Mater. **28**, 2399 (2016).

[31] M. Zulfiqar, Y. Zhao, G. Li, S. Nazir, and J. Ni, J. Phys. Chem. C **120**, 25030 (2016).

[32] X. Lin, J. C. Lu, Y. Shao, Y. Y. Zhang, X. Wu, J. B. Pan, L. Gao, S. Y. Zhu, K. Qian, Y. F. Zhang, D. L. Bao, L. F. Li, Y. Q. Wang, Z. L. Liu, J. T. Sun, T. Lei, C. Liu, J. O. Wang, K. Ibrahim, D. N. Leonard, W. Zhou, H. M. Guo, Y. L. Wang, S. X. Du, S. T. Pantelides, and H.-J. Gao, Nat. Mater., doi:10.1038/nmat4915.

[33] H.-J. Noh, J. Jeong, E.-J. Cho, K. Kim, B. I. Min, and B.-G. Park, Phys. Rev. Lett. **119**, 016401 (2017).

[34] Y. Liu, J.-Z. Zhao, L. Yu, C.-T. Lin, A.-J. Liang, C. Hu, Y. Ding, Y. Xu, S.-L. He, L. Zhao, G.-D. Liu, X.-L. Dong, J. Zhang, C.-T. Chen, Z.-Y. Xu, H.-M. Weng, X. Dai, Z. Fang, and X.-J. Zhou, Chin. Phys. Lett. **32**, 067303 (2015).

[35] P. Giannozzi, S. Baroni, N. Bonini, M. Calandra, R. Car, C. Cavazzoni, D. Ceresoli, G. L. Chiarotti, M. Cococcioni, I. Dabo, A. D. Corso, S. Gironcoli, S. Fabris, G. Fratesi, R. Gebauer, U. Gerstmann, C. Gougoussis, A. Kokalj, M. Lazzeri, L. M. Samos, N. Marzari, F. Mauri, R. Mazzarello, S. Paolini, A. Pasquarello, L. Paulatto, C. Sbraccia, S. Scandolo, G. Sclauzero, A. P. Seitsonen, A. Smogunov, P. Umari, and R. M. Wentzcovitch, J. Phys.: Condens. Matter **21**, 395502 (2009).

[36] D. M. Ceperley and B. J. Alder, Phys. Rev. Lett. **45**, 566 (1980).

[37] J. P. Perdew and A. Zunger, Phys. Rev. B **23**, 5048 (1981).

[38] S. Baroni, S. D. Gironcoli, A. D. Corso, and P. Giannozzi, Rev. Mod. Phys. **73**, 515 (2001).

[39] G. M. Eliashberg, ZhETF **38**, 966 (1960) [Sov. Phys. JETP **11**, 696 (1960)].

[40] P. B. Allen and B. Mitrovic, Solid State Phys. **37**, 1 (1983).

[41] See Supplemental Material at http://link.aps.org/supplemental/10.1103/PhysRevMaterials.1.074804 for details of electron-phonon coupling formalism, band structures, phonon dispersions, Eliashberg spectral function, and Wannier90 orbits.

[42] F. Gronvold, H. Haraldsen, and A. Kjekshus, Acta Chem. Scand. **14**, 1879 (1960).

[43] S. Furuseth, K. Selte, and A. Kjekshus, Acta Chem. Scand. **19**, 1 (1965).

[44] G. Kliche, J. Solid State Chem. **56**, 26 (1985).

[45] G Y Guo and W Y Liang, J. Phys. C: Solid State Phys. **19**, 995 (1986).

[46] S. Baroni, P. Giannozzi, and E. Isaev, Rev. Mineral. Geochem. **71**, 39 (2010).

[47] Y. S. Hor, A. J. Williams, J. G. Checkelsky, P. Roushan, J. Seo, Q. Xu, H. W. Zandbergen, A. Yazdani, N. P. Ong, and R. J. Cava, Phys. Rev. Lett. **104**, 057001 (2010).

[48] L. A. Wray, S.-Y. Xu, Y. Xia, Y. S. Hor, D. Qian, A. V. Fedorov, H. Lin, A. Bansil, R. J. Cava, and M. Z. Hasan, Nat. Phys. **6**, 855 (2010).

[49] X.-L. Zhang and W.-M. Liu, Sci. Rep. **5**, 8964 (2015).

[50] C. Cheng, J.-T. Sun, H. Liu, H.-X. Fu, J. Zhang, X.-R. Chen, and S. Meng, 2D Mater **4**, 025032 (2017).

[51] N. Marzari and D. Vanderbilt, Phys. Rev. B **56**, 12847 (1997).

[52] A. A. Mostofi, J. R. Yates, Y.-S. Lee, I. Souza, D. Vanderbilt, and N. Marzari, Comput. Phys. Commun. **178**, 685 (2008).

[53] M. D. Johannes and I. I. Mazin, Phys. Rev. B **77**, 165135 (2008).

[54] J. Bardeen, L. Cooper, and J. Schrieffer, Phys. Rev. **106**, 162 (1957).

[55] J. Bardeen, L. Cooper, and J. Schrieffer, Phys. Rev. **108**, 1175 (1957).

[56] A. B. Migdal, ZhETF **34**, 1438 (1958) [Sov. Phys. JETP **34**, 996 (1958)].

[57] W. L. McMillan, Phys. Rev. **167**, 331 (1968).

[58] P. B. Allen, Phys. Rev. B **6**, 2577 (1972).

[59] P. B. Allen and R. Dynes, Phys. Rev. B **12**, 905 (1975).

[60] P. González-Castelazo, R. de Coss-Martínez, O. De la Peña-Seaman, R. Heid, and K.-P. Bohnen, Phys. Rev. B **93**, 104512 (2016).

[61] E. S. Penev, A. Kutana, and B. I. Yakobson, Nano Lett. **16**, 2522 (2016).